Disintegration of fluids under supercritical conditions from mixing layer studies

N. Okong'o and J. Bellan

Jet Propulsion Laboratory, California Institute of Technology, Pasadena, CA 91109-8099

Databases of transitional states obtained from Direct Numerical Simulations (DNS) of temporal, supercritical mixing layers for two species systems, O_2/H_2 and C_7H_{16}/N_2, are analyzed to elucidate species-specific turbulence aspects and features of fluid disintegration. Although the evolution of all layers is characterized by the formation of high-density-gradient magnitude (HDGM) regions, due to the specified, smaller initial density stratification, the C_7H_{16}/N_2 layers display higher growth and increased global molecular mixing as well as larger turbulence levels than comparable O_2/H_2 layers. The area production of a fluid front perpendicular to the mass fraction gradient is calculated in a coordinate system moving with the relative velocity between the front and the flow. On a cross-stream local basis, the C_7H_{16}/N_2 layers produce more area, and area production increases with smaller perturbation wavelengths combined with larger initial Reynolds numbers.

1. Introduction

Supercritical fluids are of great interest in extraction processes as well as in propulsion devices such as liquid rockets, advanced gas-turbine and diesel engines. A substance is defined to be in a supercritical state when at a thermodynamic pressure (p) or temperature (T) exceeding the critical (subscript c) value (p_c or T_c) [1], in which state only one phase can exist [2]; the detailed explanation for the choice of this definition was provided by Harstad and Bellan [3]. In the practical situations of interest to the present study, fluid enters a chamber that is pressurized above the critical pressure of the injected fluid. The injected fluid then mixes in a highly turbulent manner with the chamber fluid and disintegrates into smaller parcels which participate in subsequent ignition and combustion. Clearly, fluid disintegration and turbulent mixing play a crucial role in determining the size and composition of the parcels of fluid, and consequently the efficiency of combustion.

Past the critical point of the fluid (where material liquid-vapor surfaces no longer exist), jet disintegration assumes the aspect of what Chehroudi et al. [4] call 'fingers', or 'comb-like structures' at transcritical conditions, having an increasingly gaseous appearance with increasing p; these experiments were conducted with N_2/N_2, $N_2/(CO+N_2)$, He/N_2 and O_2/N_2. Similar experimental evidence was produced by Mayer et al. [5, 6] for O_2 disintegration. Raman scattering measurements of the radial density in free N_2 jets at 4 MPa by Oschwald and Schik [7] showed sharp profiles independent of the injection temperature, indicating the occurrence of sharp density gradients. Regions of high density-gradient-magnitude (acronym HDGM) were also shown to exist in Direct Numerical Simulations (DNS) of

both pre-transitional [8] and transitional [9, 10] supercritical binary-species mixing layers. These HDGM regions were found to be the venues for high dissipation (entropy production) [9, 10], with most of the dissipation due to species-mass flux and minimal dissipation from viscous effects. The location of the highest dissipation in the HDGM regions was attributed to the sharp density stratification being very effective at damping turbulent eddies [11, 12], because it is qualitatively similar to a rigid flat plate. However, there is still uncertainty as to the fundamental connection between the HDGM regions and area production during fluid disintegration [13]. In connection to fluid disintegration, area production is defined as the increase in area of fluid fronts perpendicular to the mass fraction gradient. This study focusses on the area production in supercritical mixing layers and its relationship to other individual characteristics of the layers.

2. Highlights of the supercritical DNS

The conservation equations originate in Keizer's [14] fluctuation-dissipation theory which is consistent with non-equilibrium thermodynamics, converges to kinetic theory in the low-pressure limit and relates fluxes and forces from first principles. There are three primary differences between existing mixing-layer low-pressure equations and the equations used to generate the present database: (1) The flux matrix here contains Soret and Dufour effects in the species-mass and heat fluxes, respectively, in addition to Fick's diffusion and Fourier terms. This means that both of these fluxes contain terms that are proportional to ∇T, ∇Y (where Y is the species mass fraction), and ∇p (see details in [9, 10]). (2) p is calculated from the well-known Peng-Robinson equation of state (EOS). Consistently, all thermodynamic quantities are calculated from the EOS, including the important mass diffusion coefficient, α_D, which measures the mixture non-ideality. α_D multiplies the diffusivity D in the Fick's term, thereby modifying the species diffusivity; for ideal mixtures $\alpha_D = 1$ and the low-pressure perfect-gas situation is recovered, however, for non-ideal mixtures $0 \leqslant \alpha_D < 1$, which means that species diffusion is impeded compared to perfect gases. (3) The viscosity, the Schmidt number and the Prandtl number were calculated from high-pressure single-species transport properties using mixing rules, as in Harstad and Bellan [15]. The calculated values were correlated as functions of the thermodynamic variables, and these correlations were then used to compute D and the thermal conductivity.

The configuration is that of a three-dimensional, temporally developing binary-species mixing layer having the streamwise (x_1), cross-stream (x_2) and spanwise (x_3) coordinates. The layer is not x_2-symmetric in extent so as to accommodate the larger growth in the lighter fluid (H_2 or N_2) side, stream 1. The free-stream density (ρ_1 or ρ_2) is calculated for each pure species at its free-stream temperature (T_1 or T_2) and at the initial uniform pressure (p_0). The vorticity thickness is defined as $\delta_\omega(t) = \Delta U_0 / \left(\partial \langle u_1 \rangle / \partial x_2\right)_{max}$ where $\langle u_1 \rangle$ is the (x_1, x_3) planar average of the streamwise velocity, and $\Delta U_0 = U_1 - U_2$ is the velocity difference across the layer. U_1 and U_2 are functions of the ratio of the speeds of sound of the free streams, of ρ_1/ρ_2, possibly of Z_1/Z_2 where $Z = p/(\rho T R_u/m)$ is the compression factor which indicates departures from perfect gas ($Z = 1$) behavior (R_u is the universal gas constant and m is the mixture molar weight), and of the convective Mach number $M_{c,0}$ whose specification therefore determines ΔU_0. Given the initial streamwise velocity profile u_1 based on U_1 and U_2, $\left(\partial \langle u_1 \rangle / \partial x_2\right)_{max}$ and hence $\delta_{\omega,0} \equiv \delta_\omega(0)$ are calculated. The specified value of the initial flow Reynolds number, $\mathrm{Re}_0 = [0.5(\rho_1 + \rho_2)\Delta U_0 \delta_{\omega,0}]/\mu_R$, is then used to calculate the reference viscosity μ_R. Careful considerations regarding match-

Run	Re_0	ρ_2/ρ_1	$\lambda_1/\delta_{\omega,0}$	F_{3D}	$L_1 \times L_2 \times L_3$	$N_1 \times N_2 \times N_3$	$\mathrm{Re}_{m,tr}$	t^*_{tr}
OH500	500	24.51	10.61	0.025	0.291×0.291×0.1746	352×352×208	1772	290
OH550	550	24.40	10.35	0.025	0.284×0.284×0.17	352×352×208	1907	270
OH750	750	24.40	7.29	0.05	0.2×0.2×0.12	352×352×208	1507	150
HN500	500	12.88	7.29	0.05	0.2×0.232×0.12	240×288×144	1250	155
HN600	600	12.88	7.29	0.05	0.2×0.232×0.12	288×336×176	1452	135
HN800	800	12.88	4.57	0.05	0.125×0.148×0.075	240×272×144	1258	100

Table 1: Listing of the simulations and associated resolution for O_2/H_2 (OH) and C_7H_{16}/N_2 (HN) mixing layers. L_i, the domain size in the i^{th} direction, is in meters. N_i is the number of grid points in the i^{th} direction. For all layers, $M_{c,0}$ = 0.4, L_1=4λ_1, $\delta_{\omega,0}$=6.859×10^{-3} m and F_{2D}=0.1. The other initial conditions are: p_0=100atm (OH), 60atm (HN); p_r=2.01 (O_2), 2.22 (C_7H_{16}); T_1=287K (OH500), 600K (OH550, OH750), 1000K (HN); T_2=235K (OH500), 400K (OH550, OH750), 600K (HN); $|\rho_2 U_2| \,/\, |\rho_1 U_1|$=4.951 (OH500), 5.001 (OH550,OH750), 5.276 (HN). The subscript tr denotes the transitional time.

ing of the initial conditions between the two binary-species systems while still addressing regimes of practical interest [16] leads to the matching of the reduced pressure $p_r = p/p_c$ of the heavier fluid and of the momentum ratio of the layers as shown in Table 1 listing all simulations considered. The simulations were initiated with four streamwise and spanwise vortices, and a vorticity perturbation of wavelength λ_1 and of amplitude F_{2D} in the streamwise direction and F_{3D} in the spanwise direction induced two pairings to produce an ultimate vortex. The layers were perturbed either at the incompressible most unstable wavelength $\lambda_1/\delta_{\omega,0} = 7.29$, or at the compressible most unstable wavelength (10.61 or 10.35), or at the estimated smallest unstable wavelength (4.57), all obtained from an inviscid linear analysis.

The conservation equations were numerically solved using fourth-order explicit Runge-Kutta time integration and a sixth-order compact scheme with eighth-order filter for spatial derivatives; for numerical stability, filtering is applied at interior points only. The computations were parallelized using three-dimensional domain decomposition and message passing, and an efficient parallel tridiagonal solver.

3. Global Growth and Mixing

A fundamental characteristic of mixing layers is their growth, which can be measured using the momentum thickness, here defined as

$$\delta_m = \frac{-1}{(\theta_1 - \theta_2)^2} \int_{-L_{2,\min}}^{L_{2,\max}} (\theta_2 + \langle \rho u_1 \rangle)(\theta_1 + \langle \rho u_1 \rangle)\, dx_2 \qquad (1)$$

with $\theta_1 = \langle \rho u_1 \rangle_{x_2 = L_{2,\max}}$ and $\theta_2 = \langle \rho u_1 \rangle_{x_2 = L_{2,\min}}$, where $L_{2,\min} = -L_2/3$ and $L_{2,\max} = 2L_2/3$. While the growth is mostly a consequence of entrainment, the product thickness defined as $\delta_p = \int\int\int_V \rho Y_p dV$ in mass units, where $Y_p = 2\min(Y_1, Y_2)$, is a direct consequence of molecular mixing. $\delta_m/\delta_{\omega,0}$ is illustrated as a function of the non-dimensional time $t^* = t\Delta U_0/\delta_{\omega,0}$ in Fig. 1a for all simulations. All layers roll up and pair twice, however, the C_7H_{16}/N_2 layers display a drastic increase in $\delta_m/\delta_{\omega,0}$ after the first pairing, whereas their O_2/H_2 counterpart tend to grow more slowly. The drastic growth of the C_7H_{16}/N_2 layers compared to the O_2/H_2 ones is attributed to the smaller initial density stratification of the former. Not surprisingly, $\delta_p/\delta_{p,0}$, depicted in Fig. 1b displays a much

larger growth for C_7H_{16}/N_2 than for O_2/H_2 as a function of t^*, meaning that global molecular mixing is much more intense. Illustrated in Fig. 1c is the non-dimensional positive spanwise vorticity, $\left\langle\left\langle\omega_3^+\right\rangle\right\rangle(\delta_{\omega,0}/\Delta U_0)$ where $\langle\langle\rangle\rangle$ denotes volume averaging, which is indicative of small turbulent scale formation considering that due to the initial mean velocity profile, the initial spanwise vorticity is negative. The non-dimensional enstrophy, $\langle\langle\omega_i\omega_i\rangle\rangle(\delta_{\omega,0}/\Delta U_0)^2$, is shown in Fig. 1d and is a manifestation of stretching and tilting, which is the mechanism primarily responsible for the formation of small scales. For all simulations, $\left\langle\left\langle\omega_3^+\right\rangle\right\rangle(\delta_{\omega,0}/\Delta U_0)$ increases from the null value once the layer roll-up is completed; for each of the set of species, the layer perturbed at the shortest wavelength exhibits the earliest roll-up and highest $\left\langle\left\langle\omega_3^+\right\rangle\right\rangle(\delta_{\omega,0}/\Delta U_0)$ maximum growth. Noticeably, the two O_2/H_2 layers perturbed at the most unstable wavelength and having a smaller Re_0 display a delayed roll-up with respect to all other layers. Comparing the O_2/H_2 and C_7H_{16}/N_2 layers, one observes a drastically reduced $\left\langle\left\langle\omega_3^+\right\rangle\right\rangle(\delta_{\omega,0}/\Delta U_0)$ augmentation rate for the former compared to the latter (with particular significance for the OH500 and HN500 layers, which have the same Re_0) indicating a reduced layer growth rate. All curves exhibit local peaks at the first pairing; however, $\left\langle\left\langle\omega_3^+\right\rangle\right\rangle(\delta_{\omega,0}/\Delta U_0)$ increases following the first pairing of the C_7H_{16}/N_2 layers but decreases for the O_2/H_2 layers. Moreover, $\left\langle\left\langle\omega_3^+\right\rangle\right\rangle(\delta_{\omega,0}/\Delta U_0)$ is considerably smaller for the O_2/H_2 layer compared to the equivalent C_7H_{16}/N_2 ones, indicating that turbulence for the former is substantially reduced with respect to the latter. The enstrophy variation is consistent with this physical picture, displaying reduced levels for the O_2/H_2 layers when compared to the C_7H_{16}/N_2 ones. The largest enstrophy among O_2/H_2 layers corresponds to the one exhibiting the earliest roll-up and maximum positive spanwise vorticity.

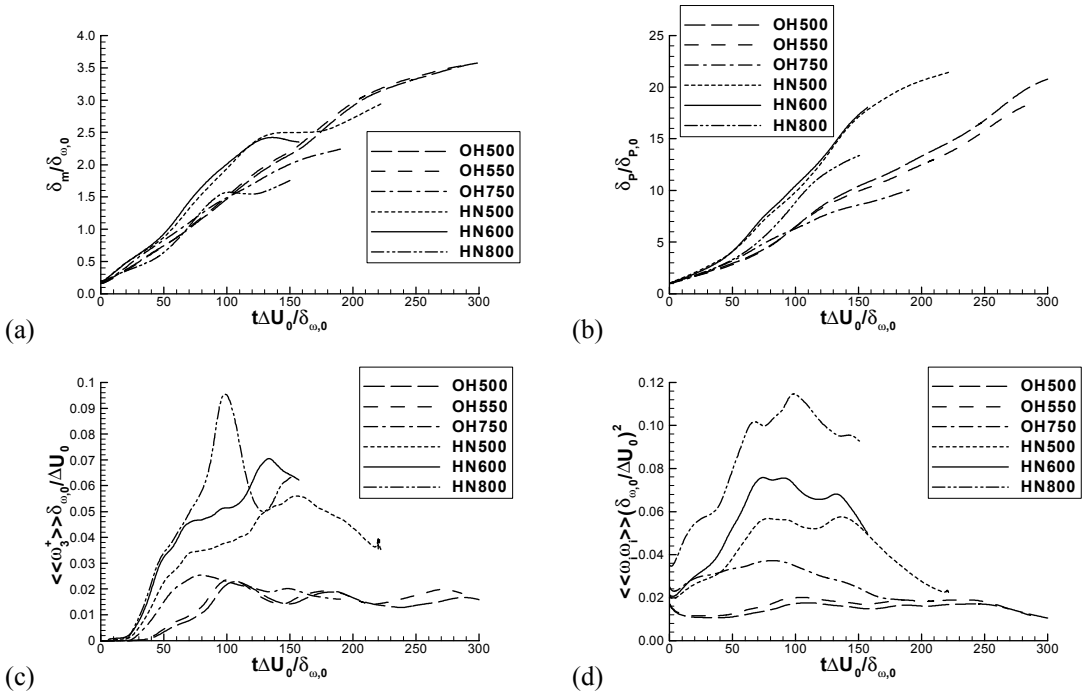

Fig. 1: Non-dimensionalized (a) momentum thickness, (b) product thickness, (c) global positive spanwise vorticity, and (d) enstrophy, all versus $t^* = t/(\Delta U_0/\delta_{\omega,0})$.

4. Area production

For a fluid front of area A, oriented perpendicular to $\zeta \equiv \nabla Y_2$ (species 2 is C_7H_{16} or O_2) and in a coordinate system moving with the relative velocity between the front and the flow, the stretch of the front is [17]

$$(1/A)\,(dA/dt) = -\left(\zeta_i \zeta_j S_{ij}\right) / \left(\zeta_k \zeta_k\right) + S_{kk}, \tag{2}$$

where the normal to the front is $n_i = -\zeta_i / \sqrt{\zeta_k \zeta_k}$ and S_{ij} is the strain rate.

An examination of the braid-plane contours of $(1/A)\,(dA/dt)$ for all layers at their transitional states (not shown) reveals that much of the area-production activity is spatially concentrated at the edge of the coherent vortices, with substantial contribution from the interior of the mixing layer; thus, both large and small scales contribute to $(1/A)\,(dA/dt)$, which exhibits both positive and negative local regions. To quantify the area creation, depicted in Fig. 2 are the homogeneous-plane average (Fig. 2a) and RMS (Fig. 2b) of $(1/A)\,(dA/dt)$ for all layers. The $(1/A)\,(dA/dt)$ average is overwhelmingly positive, with most area creation occurring inside the layers and on the lighter fluid side. Both the average and the RMS of C_7H_{16}/N_2 layers is about a factor of two larger than that of their O_2/H_2 counterpart, indicating that fluid disintegration is more effective and that fluctuations in the domain are much larger for the C_7H_{16}/N_2 layers. This finding regarding the magnitude of $(1/A)\,(dA/dt)$ averages for the two layer types is attributed to the smaller initial density stratification, $|\nabla\rho|\,\delta_{\omega,0}/\Delta\rho_0$, and the larger $(1/A)\,(dA/dt)$ RMS is conjectured to result from the complex interaction between the strength of the HDGM regions as measured by the value of $|\nabla\rho|\,\delta_{\omega,0}/\Delta\rho_0$ and the extent of their distribution in the domain. Essentially, in the O_2/H_2 layers there is globally less area production, but the area is created in a more spatially homogeneous manner that in their C_7H_{16}/N_2 counterpart. Also, area production seems uncorrelated with the magnitude of Re_m (see Table 1). Noteworthy, layers perturbed with a smaller $\lambda_1/\delta_{\omega,0}$ and having a larger Re_0 create more area on a cross-stream local basis, independent of the species system; this finding represents a first step towards area production control in turbulent supercritical fluids.

An assessment of the relative contributions of the strain and dilatation contributions to $(1/A)\,(dA/dt)$ was made by computing the budget of eq. 2 for all layers. For illustrative purposes, the results for the HN800 layer are presented in Fig. 3, which is typical of all layers. Clearly, the dominant contribution to the area production comes from the strain term, motivating its further examination.

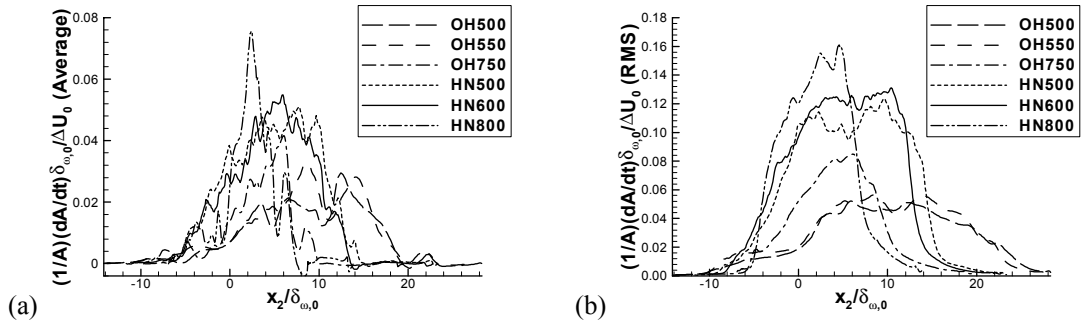

(a) (b)

Fig. 2: $(1/A)\,(dA/dt)$ at the respective transitional states: (a) average and (b) RMS in (x_1, x_3) planes for all layers listed in Table 1.

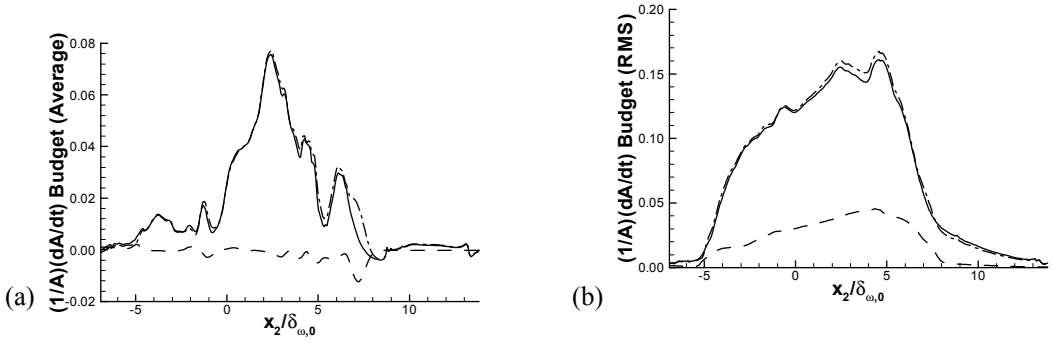

Fig. 3: Budget of $(1/A)\,(dA/dt)$ at transition: (a) average and (b) RMS in (x_1, x_3) planes for the HN800 layer.– · – · – · – $[(-\zeta_i\zeta_j S_{ij})\,/\,(\zeta_k\zeta_k)]\,(\delta_{\omega,0}/\Delta U_0)$; – – – – – $S_{kk}\,(\delta_{\omega,0}/\Delta U_0)$; ———— $(1/A)\,(dA/dt)\,(\delta_{\omega,0}/\Delta U_0)$.

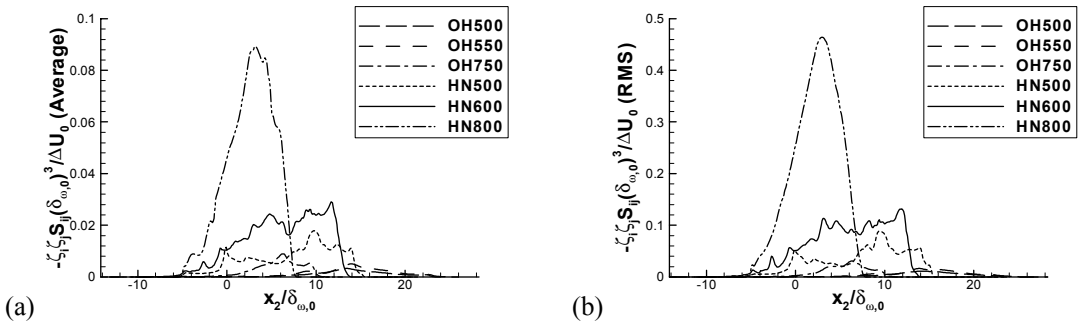

Fig. 4: $(-\zeta_i\zeta_j S_{ij})$ at the respective transitional states: (a) average and (b) RMS in (x_1, x_3) planes for all layers listed in Table 1.

To determine the respective influence of the numerator and denominator of $(-\zeta_i\zeta_j S_{ij})\,/\,(\zeta_k\zeta_k)$, we illustrated them (averages and RMS of homogeneous planar averages) in Figs. 4 and 5. The plots in Fig. 4 show that the HN800 layer is significantly more active than the other layers, and the OH500 and OH550 layers are the least active, similar to the findings for $(1/A)\,(dA/dt)$. The location of the $(1/A)\,(dA/dt)$ peak correlates to that of $(-\zeta_i\zeta_j S_{ij})$, although the curves have drastically different profiles. In contrast, $|\zeta| = \sqrt{\zeta_k\zeta_k}$, plotted in Fig. 5 does not correlate with the $(1/A)\,(dA/dt)$ activity. This means that the direction of ζ rather than its magnitude has a strong influence on area production.

To examine the origin of the different behavior of $(-\zeta_i\zeta_j S_{ij})$, a differential equation for it was derived,

$$\begin{aligned}\frac{D}{Dt}\left(-\zeta_i\zeta_j S_{ij}\right) &= 2\frac{\partial u_k}{\partial x_i}\zeta_j\zeta_k S_{ij} + S_{ik}S_{kj}\zeta_i\zeta_j + \frac{1}{4}\left(\omega_i\zeta_i\omega_j\zeta_j - \omega_i\omega_i\zeta_j\zeta_j\right) \\ &\quad +\zeta_i\zeta_j\frac{\partial}{\partial x_i}\left(\frac{1}{\rho}\frac{\partial p}{\partial x_j}\right) + 2\zeta_i S_{ij}\frac{\partial}{\partial x_j}\left(\frac{1}{\rho}\frac{\partial j_{2k}}{\partial x_k}\right) - \zeta_i\zeta_j\frac{\partial}{\partial x_i}\left(\frac{1}{\rho}\frac{\partial \tau_{jk}}{\partial x_k}\right) \quad (3)\end{aligned}$$

and its budget analyzed. It was found that most of the activity occurs on the light fluid side of the layer, whether for the average or for the RMS. Compared to the C_7H_{16}/N_2 layers, the average and RMS are for O_2/H_2 layers one and two orders of magnitude smaller, respectively, indicating a more subdued activity. Consistent with the $(1/A)\,(dA/dt)$ results,

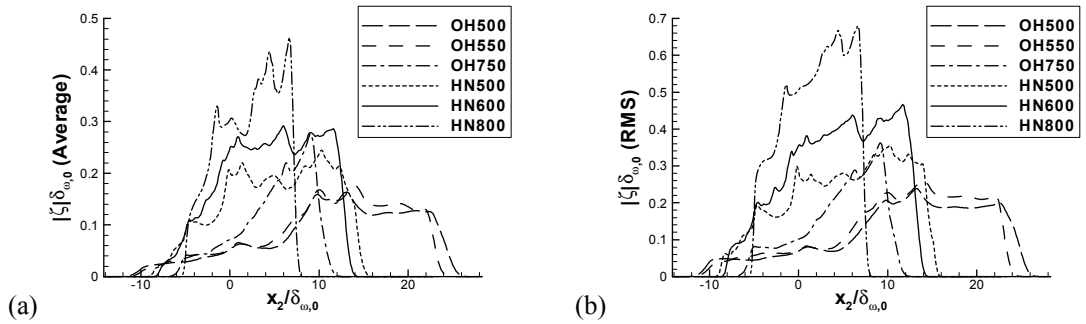

Fig. 5: Mass fraction gradient magnitude at the respective transitional states: (a) average and (b) RMS in (x_1, x_3) planes for all layers listed in Table 1.

the HN800 layer is the most active. For the average, strain and convection effects lead to production of area, whereas rotational and species mass flux (j_{2k}) effects destroy it; since the front is oriented perpendicular to ζ, the species mass flux tends to decrease ζ, explaining the decrease in $(-\zeta_i\zeta_j S_{ij})$. ∇p can either destroy area, or produce it near the light fluid free-stream; the viscous stress (τ_{jk}) effect is negligible. Generally, on average the strain term balances the rotational term while the mass flux term counteracts the convective term; the RMS of each pair of terms has comparable magnitude and similar location of peaks. For all layers, the ∇p term has the second smallest contribution to the average. However, in contrast to O_2/H_2 layers, most of the RMS for C_7H_{16}/N_2 layers is dominated by the ∇p term, while the other contributions, with the exception of the much smaller viscous term, are equivalent. For O_2/H_2 layers, the mass flux term dominates the RMS, and is rivaled by convective, strain and rotational effects, with the ∇p term contribution being small and decreasing with combined decreasing $\lambda_1/\delta_{\omega,0}$ and increasing Re_0, which represents an opposite result to that seen for the C_7H_{16}/N_2 simulations. Superimposing braid and between-the-braid contour plots of $|\nabla\rho|$, $|\nabla p|$ and $\zeta\zeta\nabla\left(\nabla p/\rho\right)$ led to the conclusion that whereas in the C_7H_{16}/N_2 layers the regions of $\zeta\zeta\nabla\left(\nabla p/\rho\right)$ activity coincided with the overlap of the significant $|\nabla p|$ with the HDGM regions, no such behavior existed for the O_2/H_2 layers. Considering that for the (p,T) conditions of the O_2/H_2 layers both fluids are quite close to perfect gases [10] compared to the C_7H_{16}/N_2 layers where strong departures from perfect gas behavior are exhibited [9], [8], the large contribution of $\zeta\zeta\nabla\left(\nabla p/\rho\right)$ to the $(-\zeta_i\zeta_j S_{ij})$ RMS is attributed to the strong p coupling with ρ through the real gas EOS.

5. Conclusions

Databases obtained from Direct Numerical Simulations of binary-species supercritical temporal mixing layers were compared to investigate fluid disintegration. The simulations were performed for O_2/H_2 and C_7H_{16}/N_2 layers at approximately the same reduced pressure of 2 with respect to the pure heavier species and similar momentum ratios. Global characteristics of the layers showed that the momentum thickness and product thickness growth is substantially reduced for the O_2/H_2 layers compared to the C_7H_{16}/N_2 ones, and that the levels of the positive spanwise vorticity and the enstrophy for the O_2/H_2 layers were also diminished, indicating less turbulence activity. These results are attributed to the much larger initial density stratification of the O_2/H_2 layers, which delays entrainment and pair-

ing. The area production of fluid fronts perpendicular to the scalar gradient was examined in a coordinate system moving with the relative velocity between the front and the flow. Smaller wavelength initial perturbations combined with larger initial vorticity-thickness based Reynolds numbers led to enlarged area creation. Area production for C_7H_{16}/N_2 layers was found to be larger than for the O_2/H_2 layers, this being attributed to the smaller initial density stratification of the C_7H_{16}/N_2 layers as well as to the manifestation of the strong pressure/density coupling through the equation of state, resulting from considerable departures from perfect gas and ideal mixture behavior. These findings highlight the importance of real gas thermodynamics in the modeling of supercritical turbulent mixing.

Acknowledgment

This work was conducted at the Jet Propulsion Laboratory (JPL), California Institute of Technology (Caltech) and sponsored by the National Aeronautics and Space Administration (NASA), Marshall Space Flight Center under the direction of Dr. John Hutt, the Air Force Office of Scientific Research under the direction of Dr. Julian Tishkoff, and the Army Research Office under the direction of Dr. David Mann, through interagency agreements with NASA. Computational resources were provided by the JPL Supercomputing Center.

6. References

[1] Prausnitz J, Lichtenthaler R and de Azevedo E 1986 *Molecular Thermodynamics for Fluid-Phase Equilibrium*(Prentice-Hall)

[2] Hirshfelder J, Curtis C and Bird R 1964 *Molecular Theory of Gases and Liquids* (John Wiley and Sons)

[3] Harstad K and Bellan J 2001 *Combustion and Flame* **127**(1–2) 1861-79

[4] Chehroudi B, Talley D and Coy E 1999 AIAA Paper 99-0206

[5] Mayer W, Schik A, Schweitzer C and Schaffler M 1996 AIAA Paper 96-2620

[6] Mayer W, Ivancic B, Schik A and Hornung U 1998 AIAA Paper 98-3685

[7] Oschwald M and Schik A 1999 *Experiments in Fluids* **27** 497-506

[8] Miller R, Harstad Kand Bellan J 2001 *Journal of Fluid Mechanics* **436** 1-39

[9] Okong'o N and Bellan J 2002 *Journal of Fluid Mechanics* **464** 1-34

[10]Okong'o N, Harstad K and Bellan J 2002 *AIAA Journal* **40**(5) 914-26

[11]Hannoun I, Fernando H and List E 1988 *Journal of Fluid Mechanics* **189** 189-209

[12]Briggs D, Ferziger J, Koseff J and Monismith S 1998 *Journal of Fluid Mechanics* **354** 175-208

[13]Bellan J 2000 *Progress in Energy and Combustion Science* **26**(4–6) 329-66

[14]Keizer J 1987 *Statistical Thermodynamics of Nonequilibrium Processes* (Springer-Verlag, New York)

[15]Harstad K and Bellan J 1998 *International Journal of Heat and Mass Transfer* **41** 3537-50

[16]Okong'o N and Bellan J 2003 Turbulence and area production in binary-species, supercritical, transitional mixing layers, submitted to *Physics of Fluids*

[17]Candel S and Poinsot T 1990 *Combustion Science and Technology* **70** 1-15